Research Square

Preprints are preliminary reports that have not undergone peer review.
They should not be considered conclusive, used to inform clinical practice,
or referenced by the media as validated information.

Diagnostic value of dual-energy CT in differential diagnosis of osteoblastic metastasis and bone islands

Jinfang Shi
Chongqing University Cancer Hospital
Junhua Shao
Chongqing University Cancer Hospital
Meng Lin
Chongqing University Cancer Hospital
Yao Huang
Chongqing University
Lu Wang
Chongqing University Cancer Hospital
Huifang Chen
Chongqing University Cancer Hospital
Ying Cao
Chongqing University
Jing Zhang
Chongqing University Cancer Hospital
Yong Tan
Chongqing University Cancer Hospital
Hong Yu
Chongqing University Cancer Hospital
Xiaoxia Wang
Chongqing University Cancer Hospital
Jiuquan Zhang
zhangjq_radiol@foxmail.com

Chongqing University Cancer Hospital

Research Article

Keywords: Bone neoplasms, Osteogenesis, Spinal diseases, Differential diagnosis

Posted Date: April 10th, 2026

DOI: https://doi.org/10.21203/rs.3.rs-8983390/v1

License: This work is licensed under a Creative Commons Attribution 4.0 International License.
Read Full License

Additional Declarations: No competing interests reported.

Abstract

Background

To evaluate the performance of multiple quantitative parameters derived from three-phase dual-energy CT (DECT) in the differential diagnosis of osteoblastic metastasis (OBM) from bone islands (BI).

Methods

In this retrospective study, patients who underwent contrast-enhanced CT scan and were diagnosed with OBM or BI between April 2019 to December 2022 were included. Multiple quantitative parameters including CT attenuation (CTa), iodine concentration (IC), slope of the spectral Hounsfield unit curve (λ_{Hu}), electron density (Rho), effective atomic number (Z_{eff}) (all derived from three-phase DECT scan) and virtual non-calcium (VNCa) (derived from pre-contrast DECT scan), then compared between OBM and BI groups. The diagnostic performance was evaluated using receiver operator characteristic (ROC) curve.

Results

A total of 125 patients with malignant tumors were enrolled, including 51 patients with 124 OBM and 74 patients with 119 BI. VNCa of OBM was significantly higher than BI, whereas other DECT quantitative parameters of OBM were significantly lower than BI (all $P < 0.001$). The parameters extracted from different phases were highly correlated with each other both in the OBM group (r, 0.637–0.862) and BI group (r, 0.490–0.903), except VNCa. The three-phase DECT quantitative parameters performed well in identifying both OBM and BI; in particular, VNCa achieved an excellent and stable diagnostic performance in both the training group and testing group with AUC 1.00, sensitivity 100.0%, specificity 100.0%, and accuracy 100.0% ($P < 0.001$).

Conclusions

DECT derived multiple quantitative parameters that demonstrated excellent performance in differentiating OBM from BI. Notably, VNCa could completely distinguish between the OBM and BI.

Introduction

Around 20–70% of patients with primary malignant tumors develop bone metastasis (BM), of which 30–50% are spinal metastasis [1–3]. BM often causes pathological fracture, spinal cord compression and hypercalcaemia among other skeletal complications, resulting in the loss of social function, decline in quality of life, increase in medical expenses and reduced survival rate [4–6]. The European Society for Medical Oncology (ESMO) Clinical Practice Guidelines recommend the use of systemic therapy

combined with local therapy for the BM [5]. BM is usually divided into osteoblastic metastasis (OBM) and osteolytic metastasis. OBM present as a focal dense sclerosing osteopathy [7]. Bone islands (BI) is a common benign lesion of the vertebral body similar to OBM; they are often found during CT examinations and do not require treatment [8; 9]. For patients with malignant tumors, accurate differentiation between OBM and BI plays a crucial role in clinical staging, treatment decision-making and prognosis [10–12].

Positron emission tomography (PET) and single photon emission CT (SPECT) are used in the diagnosis and monitoring of BM [5], but BI sometimes show false positives for heat uptake on PET/CT [10]. Furthermore, PET is highly radioactive and expensive and it cannot be used for dynamic monitoring. CT is the most commonly used examination tool for diagnosis and follow-up of cancer patients [11]. According to ESMO Clinical Practice Guidelines, CT can also be used to diagnose and monitor BM [5]. However, conventional CT can only provide limited diagnostic information based on a single CT attenuation (CTa).

DECT is an imaging technique that uses X-ray beams of two different energies to scan an object, thereby obtaining two datasets of different energies [13; 14]. Compared with conventional CT, the advantage of DECT is that it has multiple quantitative parameters that can provide more valuable diagnostic information for tumor evaluation in clinical practice [15; 16]. Many studies have evaluated the good diagnostic performance of DECT-derived multi-parameters for distinguishing OBM and BI, such as CTa on linear mixed images [11; 17–19] and under different virtual monoenergetic images (VMIs) [7; 20], bone densities and water densities [20], water (calcium) density, calcium (water) density and Iodine (calcium) density [7], electron density (Rho) [11], effective atomic number (Z_{eff}) [7; 11], and slope of the spectral Hounsfield unit (HU) curve (λ_{Hu}) [7; 20]. Despite this, no studies have fully investigated the performance of three-phase DECT-derived multi-parameters for the identification of OBM and BI in the same tissue sample. As an additional consideration, DECT has been proven to emit lower radiation doses while having higher imaging quality [16], so it is more suitable for long-term follow-up of patients with malignant tumors.

Here, we evaluate the performance of three-phase DECT-derived quantitative multi-parameters in the differential diagnosis of OBM and BI.

Methods

Patient Characteristics

This study was approved by the Ethics Committee of our hospital and the need for written informed consent was waived owing to the use of retrospective data. A search of radiological reports of contrast-enhanced DECT scans from April 2019 to December 2022 was performed in the hospital picture archive and communication system using the following keywords: BM, OBM, high-density bone lesions, BI and sclerotic metastasis. Inclusion criteria were as follows: (1) The primary malignant tumor of the patient

was confirmed by pathological biopsy; (2) The patient did not receive antitumor therapy prior to contrast-enhanced DECT scan. Exclusion criteria were as follows: (1) Clinical or imaging data were incomplete; (2) The diagnosis of intraosseous high-density lesions was controversial; (3) Osteolytic and osteoblastic metastasis coexisted on CT. Diagnostic criteria for OBM were as follows: (1) High density intraosseous lesions; (2) Avid radiotracer uptake on SPECT/CT or PET/CT scan; (3) An increase in lesion density and/or size on 6-month or longer follow-up CT images; (4) Lack of compression fracture or pathologic fracture. Diagnostic criteria for BI were as follows: (1) Typical radiologic appearance, such as round or oblong, sclerotic, homogeneous lesions, or with a spiculated margin [18]; (2) No overt radiotracer uptake on SPECT/CT or PET-CT scan ; (3) No change in lesion size, density and shape on follow-up CT scans obtained at least 6 months later [10]. Ultimately, 51 patients with 124 lesions were enrolled in the OBM group, and 74 patients with 119 lesions were enrolled in the BI group. The inclusion and screening of patients is shown in Fig. 1.

DECT Image Acquisition

The dual-energy image data were obtained in the dual-energy mode (SOMATOM Drive; Siemens Healthineers, Forchheim, Germany), and the voltages of the high and low arena tubes were 100 kVp and sn140 kVp, respectively. An automatic exposure control system (CARE Dose4D; Siemens Healthineers) was used for all scans. Scan parameters were as follows: detector width 64 × 0.6 mm; rotation time 0.5 s/r; pitch 0.8; ADMIRE level 3; slice thickness, 1.5 mm; interlayer spacing, 1.2 mm. The iodine contrast agent (Iodixanol, 320 mg/mL iodine, HENGRUI Medicine, Jiangsu, China) was injected through the anterior cubital vein at a dosage of 1.5 mL/kg and a speed of 2.5 mL/s, and then normal saline (30 mL) was injected at the same speed. Using the threshold of the bolus-tracking technique, scanning was triggered with an additional delay of 8 seconds when the CTa of the abdominal aorta reached 100 Hu, and the venous phase was scanned after a delay of 20 seconds.

DECT Image Reconstruction and Parameter Measurement

The DECT data were post-processed by syngo.via workstation (syngo.via VB20B, Dual Energy; Siemens Healthineers). The syngo.via workstation was used to generate the iodine overlay image and Rho/Z_{eff} maps. Under the single-energy algorithm, all the original data were reconstructed into VMIs of layer thickness 1.5 mm and layer spacing 1.2 mm. Linear mixed images were reconstructed by a mixing factor of 0.5 (M_0.5; 50% of the low kVp and 50% of the high kVp spectrum). In addition, the bone marrow image was reconstructed with pre-contrast data. The principle of focus delineation was applied by selecting the largest layer of the lesion and placing a circular or oval region of interest in the center of the lesion. The measurement data included the following: (1) The CTa of VNCa was measured on the bone marrow image; (2) The CTa was measured in pre-contrast, arterial and venous phases on the linear mixed images; (3) The iodine concentration (IC) was measured in pre-contrast, arterial and venous phases on the iodine overlay image; (4) The Rho/Z_{eff} was measured in pre-contrast, arterial and venous

phases on the Rho/Z_{eff} maps; (5) The CTa was measured in pre-contrast, arterial and venous phases at the energy levels of VMIs at 40 keV and 100 keV; (6) The spectral curves were drawn in pre-contrast, arterial and venous phases, and the slope of the spectral Hounsfield unit curve (λ_{Hu}) was calculated and analyzed (40 keV and 100 keV was selected as the slope calculation point in this experiment), that is, the slope K = CT (40 keV)-CT (100 keV) / 60.

Statistical analysis

Commercial statistical software was used for statistical analysis (SPSS software, version 25.0; USA). All continuous variables were expressed as mean ± standard deviation (SD), and categorical variables were described as numbers and percentages. Chi-square tests were used to compare patient gender and lesion location. Patient age, BMI and DECT quantitative parameter features were compared using independent sample t-test or Mann-Whitney U test. Pearson's correlation was used to test the correlation between multi-parameters derived from DECT pre-contrast, arterial and venous phases. Correlation was defined as follows: $0 \leq |r| < 0.3$, indicating no correlation; $0.3 \leq |r| < 0.5$, indicating a weak correlation; $0.5 \leq |r| < 0.8$, indicating a moderate correlation; $0.8 \leq |r| \leq 1.0$, indicating a high correlation. In this study, lesions were randomly divided into training and testing groups according to a 3:2 ratio. Then, multiple logistic regression analysis and five-fold cross validation were used to predict the differential diagnosis results. Diagnostic performance was evaluated using receiver operating characteristics (ROC) analysis. The significant difference was defined as $P < 0.05$.

Results

Participant characteristics

A total of 125 patients were enrolled in this study, including 51 patients (60.45 ± 11.83 years) with 124 OBM and 74 patients (63.01 ± 11.61 years) with 119 BI. There was no significant difference in patient gender ($P = 0.56$), age ($P = 0.23$) or BMI ($P = 0.44$) between the OBM and BI groups. The distribution of lesion locations was statistically significant ($P < 0.001$), which indicated that OBM and BI were prone to different sites. The most common location for OBM was the thoracic vertebrae (58.1%), followed by lumbar vertebrae (38.7%). The most common location for BI was the thoracic vertebrae (41.2%), followed by the pelvis (31.1%) and lumbar vertebrae (21.0%). The top three primary cancers of OBM were lung cancer (37.3%), breast cancer (31.4%), and prostate cancer (25.5%); the top two cancers of BI were lung cancer (37.8%) and breast cancer (14.9%). The clinicopathological features of all patients are shown in Table 1.

Table 1. The baseline characteristics of participants.

Characteristics	Osteoblastic metastasis (n = 51 patients)	Bone islands (n = 74 patients)	*P* value
Number of lesions	124	119	
Gender (male /female)	27/24	39/35	0.56
Age, mean ± SD, years	60.45 ± 11.83	63.01 ± 11.61	0.23
BMI, mean ± SD, kg/m^2	22.84 ± 3.85	23.37 ± 3.57	0.44
Lesion location (%) *			< 0.001
Thoracic vertebra	72 (58.1%)	49 (41.2%)	
Lumbar vertebra	48 (38.7%)	25 (21.0%)	
Cervical and Sacral vertebrae	3 (2.4%)	8 (6.7%)	
Pelvis	1 (0.8%)	37 (31.1%)	
Primary tumor type (%) #			
Lung cancer	19 (37.3%)	28 (37.8%)	
Breast cancer	16 (31.4%)	11 (14.9%)	
Esophageal cancer		5 (6.8%)	
Gastric cancer	1 (2.0%)	6 (8.1%)	
Liver cancer		3 (4.1%)	
Pancreatic cancer	1 (2.0%)	3 (4.1%)	
Colorectal cancer	1 (2.0%)	9 (12.2%)	
Renal cancer		4 (5.4%)	
Prostate cancer	13 (25.5%)	1 (1.4%)	
Others		4 (5.4%)	

Note. SD = standard deviation. * The data is the number of lesions; # The data is the number of patients.

Comparison of DECT derived multi-parameters between OBMs and BIs

The comparison of DECT quantitative parameters between OBM and BI are shown in Table 2. The results demonstrate that with the notable exception of VNCa, all other DECT quantitative parameters of OBM were significantly lower than those of BI (all $P < 0.001$, Fig. 2). Two representative patient images are shown in Fig. 3. The OBM and BI had the following parameters in pre-contrast, with OBM listed first and BI second: VNCa − 13.11 ± 66.10 / −1013.86 ± 47.22 Hu; CTa 526.70 ± 103.67 / 1030.18 ± 147.41 Hu; IC 9.38 ± 2.13 / 18.14 ± 3.19 mg/ml; λ_{Hu} 13.70 ± 3.23 / 25.86 ± 4.76 Hu/keV; Rho 314.00 ± 60.73 / 607.61 ± 98.22 and Z_{eff} 11.20 ± 0.48 / 12.61 ± 0.40. The specific parameter values of dual-phase enhancement are shown in Table 2.

Table 2
Conventional univariate analysis of DECT quantitative parameters for Osteoblastic metastasis and Bone islands.

Feature	Osteoblastic metastasis (N = 124 lesions)	Bone islands (N = 119 lesions)	t/Z value	*P* value
Pre-contrast				
VNCa (Hu)	-13.11 ± 66.10	-1013.86 ± 47.22	-14.03	< 0.001
CTa (Hu)	526.70 ± 103.67	1030.18 ± 147.41	-13.41	< 0.001
IC (mg/ml)	9.38 ± 2.13	18.14 ± 3.19	-13.18	< 0.001
λ_{Hu} (Hu/keV)	13.70 ± 3.23	25.86 ± 4.76	-12.83	< 0.001
Rho	314.00 ± 60.73	607.61 ± 98.22	-13.34	< 0.001
Z_{eff}	11.20 ± 0.48	12.61 ± 0.40	-13.23	< 0.001
Arterial phase				
CTa (Hu)	527.48 ± 114.93	1013.55 ± 155.06	-13.28	< 0.001
IC (mg/ml)	9.37 ± 2.16	16.86 ± 2.90	-13.03	< 0.001
λ_{Hu} (Hu/keV)	13.28 ± 2.80	24.42 ± 4.40	-13.07	< 0.001
Rho	321.57 ± 62.31	610.59 ± 101.90	-13.29	< 0.001
Z_{eff}	11.19 ± 0.45	12.42 ± 0.43	-12.91	< 0.001
Venous phase				
CTa (Hu)	546.87 ± 118.01	1009.31 ± 147.47	-13.27	< 0.001
IC (mg/ml)	9.72 ± 2.03	16.68 ± 2.76	-12.88	< 0.001
λ_{Hu} (Hu/keV)	14.08 ± 3.11	24.83 ± 4.11	-12.97	< 0.001
Rho	316.82 ± 60.09	608.85 ± 99.97	-13.17	< 0.001
Z_{eff}	11.24 ± 0.42	12.43 ± 0.40	-12.84	< 0.001

Note. The data is represented as means ± standard deviation. VNCa, virtual non-calcium; HU, Hounsfield unit; CTa, CT attenuation; IC, Iodine concentration; λ_{Hu}, slope of the spectral Hounsfield unit curve; Rho, electron density; Z_{eff}, effective atomic number.

Correlation between DECT derived multi-parameters

As shown in Fig. 4, in the OBM group, VNCa only had a weak correlation with some parameters (IC, r = − 0.332; λ_{Hu}, r = − 0.342; Rho, r = − 0.355) extracted from the venous phase. Interestingly, the other

parameters (CTa, IC, $\lambda_{Hu,}$ Rho, Z_{eff}) in different phases had a high correlation with each other (r, 0.637–0.862). In the BI group, VNCa was not correlated with the parameters extracted from either the arterial phase or venous phase. In contrast, most of the other parameters were highly correlated.

Model Performance

The VNCa had the highest AUC (1.00), sensitivity (100.0%), specificity (100.0%), and accuracy (100.0%) in both the training and testing groups. The next highest parameters were pre-contrast CTa and pre-contrast Z_{eff} (AUC 1.00, sensitivity 98.6–100.0%, specificity 96–100.0%, accuracy 97.2–100.0% in the training group; AUC 0.98–0.99, sensitivity 93.8–95.8%, specificity 98%, accuracy 95.9–96.9% in the testing group). Other quantitative parameters also achieved promising performance (AUC 0.97–0.99, sensitivity 91.4–100.0%, specificity 93.3–100.0%, accuracy 92.4–98.6% in the training group; AUC 0.96–0.99, sensitivity 89.6–95.8%, specificity 92.0–100.0%, accuracy 92.9–96.9% in the testing group (Table 3)). Most notably, VNCa could completely distinguish OBM from BI (Fig. 5). The ROC curves of the quantitative parameters from different phases are shown in Fig. 6.

Table 3
Classification performance of DECT quantitative parameters in the training and testing group

Pre-contrast	AUC	Sensitivity (%)	Specificity (%)	Accuracy (%)	PPV (%)	NPV (%)
VNCa (Hu)						
Training group	1.00	100.0 (70/70)	100.0 (75/75)	100.0 (145/145)	100.0 (70/70)	100.0 (75/75)
Testing group	1.00	100.0 (48/48)	100.0 (50/50)	100.0 (98/98)	100.0 (48/48)	100.0 (50/50)
CTa (Hu)						
Training group	1.00	98.6 (69/70)	98.7 (74/75)	98.6 (143/145)	98.6 (69/70)	98.7 (74/75)
Testing group	0.99	95.8 (46/48)	98.0 (49/50)	96.9 (95/98)	97.9 (46/47)	96.1 (49/51)
IC (mg/ml)						
Training group	0.99	95.7 (67/70)	98.7 (74/75)	97.2 (141/145)	98.5 (67/68)	96.1 (74/77)
Testing group	0.98	93.8 (45/48)	98.0 (49/50)	95.9 (94/98)	97.8 (45/46)	94.2 (49/52)
λ_{Hu} (Hu/keV)						
Training group	0.97	95.7 (67/70)	96.0 (72/75)	95.9 (139/145)	95.7 (67/70)	96.0 (72/75)
Testing group	0.96	89.6 (43/48)	100.0 (50/50)	95.0 (93/98)	100.0 (43/43)	90.9 (50/55)
Rho						
Training group	0.99	97.1 (68/70)	97.3 (73/75)	97.2 (141/145)	97.1 (68/70)	97.3 (73/75)
Testing group	0.99	91.7 (44/48)	100.0 (50/50)	95.9 (94/98)	100.0 (44/44)	92.6 (50/54)
Z_{eff}						
Training	1.00	98.6 (69/70)	96.0 (72/75)	97.2	95.8	98.6

Note. The data is represented as means ± standard deviation. VNCa, virtual non-calcium; HU, Hounsfield unit; CTa, CT attenuation; IC, Iodine concentration; λ_{Hu}, slope of the spectral Hounsfield unit curve; Rho, electron density; Z_{eff}, effective atomic number.

Pre-contrast	AUC	Sensitivity (%)	Specificity (%)	Accuracy (%)	PPV (%)	NPV (%)
group				(141/145)	(69/72)	(72/73)
Testing group	0.98	93.8 (45/48)	98.0 (49/50)	95.9 (94/98)	97.8 (45/46)	94.2 (49/52)
Arterial phase						
CTa (Hu)						
Training group	0.99	98.6 (69/70)	94.7 (71/75)	96.6 (140/145)	94.5 (69/73)	98.7 (71/72)
Testing group	0.99	93.8 (45/48)	100.0 (50/50)	96.9 (95/98)	100.0 (45/45)	94.3 (50/53)
IC (mg/ml)						
Training group	0.98	95.7 (67/70)	97.3 (73/75)	96.6 (140/145)	97.1 (67/69)	96.1 (73/76)
Testing group	0.98	95.8 (46/48)	92.0 (46/50)	93.9 (92/98)	92.0 (46/50)	95.8 (46/48)
λ_{Hu} (Hu/keV)						
Training group	0.97	92.9 (65/70)	97.3 (73/75)	95.2 (138/145)	97.0 (65/67)	93.6 (73/78)
Testing group	0.98	91.7 (44/48)	94.0 (47/50)	92.9 (91/98)	93.7 (44/47)	92.2 (47/51)
Rho						
Training group	0.99	97.1 (68/70)	94.7 (71/75)	95.9 (139/145)	94.4 (68/72)	97.3 (71/73)
Testing group	0.99	93.8 (45/48)	100.0 (50/50)	96.9 (95/98)	100.0 (45/45)	94.3 (50/53)
Z_{eff}						
Training group	0.98	91.4 (64/70)	93.3 (70/75)	92.4 (134/145)	92.8 (64/69)	92.1 (70/76)
Testing	0.97	95.8 (46/48)	90.0 (45/50)	92.9 (91/98)	90.2	95.7

Note. The data is represented as means ± standard deviation. VNCa, virtual non-calcium; HU, Hounsfield unit; CTa, CT attenuation; IC, Iodine concentration; λ_{Hu}, slope of the spectral Hounsfield unit curve; Rho, electron density; Z_{eff}, effective atomic number.

Pre-contrast	AUC	Sensitivity (%)	Specificity (%)	Accuracy (%)	PPV (%)	NPV (%)
group					(46/51)	(45/47)
Venous phase						
CTa (Hu)						
Training group	0.99	100.0 (70/70)	93.3 (70/75)	96.6 (140/145)	93.3 (70/75)	100.0 (70/70)
Testing group	0.98	93.8 (45/48)	100.0 (50/50)	96.9 (95/98)	100.0 (45/45)	94.3 (50/53)
IC (mg/ml)						
Training group	0.97	92.9 (65/70)	93.3 (70/75)	93.1 (135/145)	92.9 (65/70)	93.3 (70/75)
Testing group	0.97	93.8 (45/48)	98.0 (49/50)	95.9 (94/98)	97.8 (45/46)	94.2 (49/52)
λ_{Hu} (Hu/keV)						
Training group	0.99	95.7 (67/70)	96.0 (72/75)	95.9 (139/145)	95.7 (67/70)	96.0 (72/75)
Testing group	0.96	91.7 (44/48)	96.0 (48/50)	93.9 (92/98)	95.7 (44/46)	92.3 (48/52)
Rho						
Training group	0.98	91.4 (64/70)	96.0 (72/75)	93.8 (136/145)	95.5 (64/67)	92.33 (72/78)
Testing group	0.97	91.7 (44/48)	100.0 (50/50)	95.9 (94/98)	100.0 (44/44)	92.6 (50/54)
Z_{eff}						
Training group	0.98	91.4 (64/70)	96.0 (72/75)	93.8 (136/145)	95.5 (64/67)	92.3 (72/78)
Testing group	0.97	91.7 (44/48)	100.0 (50/50)	95.9 (94/98)	100.0 (44/44)	92.7 (50/54)

Note. The data is represented as means ± standard deviation. VNCa, virtual non-calcium; HU, Hounsfield unit; CTa, CT attenuation; IC, Iodine concentration; λ_{Hu}, slope of the spectral Hounsfield unit curve; Rho, electron density; Z_{eff}, effective atomic number.

Discussion

This study applied quantitative multi-parameters derived from three-phase DECT to distinguish OBM from BI. We found that, apart from VNCa, all DECT-derived quantitative parameters of OBM were significantly lower than those of BI (all $P < 0.001$). VNCa was the sole parameter that was significantly higher in OBM compared to BI ($P < 0.001$). The parameters extracted from different phases were highly correlated with each other in both the OBM and BI groups, except for VNCa. These 16 DECT quantitative parameters have high diagnostic efficiency in the differential diagnosis of OBM from BI.

Previous studies have demonstrated that OBM are more common in prostate cancer, whereas most of the BM of lung and breast cancer presents as osteolytic metastasis [21–23]. Lung cancer and breast cancer comprise the highest incidence of cancer worldwide, even higher than prostate cancer [24]. This is the reason why lung cancer and breast cancer accounted for a relatively high proportion of the primary tumors of OBM in this study. We found that the DECT-derived quantitative multi-parameters from different phases were not significantly different in the differential diagnosis of OBM and BI. Therefore, from the perspective of patient safety and economy, we recommend the use of pre-contrast images to distinguish OBM from BI.

DECT post-processing software is used to remove highly attenuated bone calcium signal from an image to obtain a VNCa image, which provides superior bone marrow imaging evaluation and can also be used for the detection of BM [15; 25]. Studies have shown that VNCa has excellent diagnostic performance in assessing bone marrow infiltration [26; 27] and is valuable for the diagnosis of BM [28–30]. In this study, we found that the VNCa of BI (− 1013.86 ± 47.22 Hu) was much lower than that of OBM (− 13.11 ± 66.10 Hu ($P < 0.001$)). This finding could be related to the pathological nature of BI and OBM. BI, also known as bone spots, are bony nodules in cancellous bone that are caused by abnormal bone development and are virtually free of osteoblasts and osteoclasts, and are purely composed of bone structures [31; 32]. Since BI only contain calcium components, after the use of VNCa technology to remove all the calcium substances in BI images there is no substance remaining. As a result, the obtained VNCa is approximately − 1000 Hu, close to the CTa of air. In contrast, OBM contain abundant tumor cells and bone-like tissue with incomplete calcium salt deposition [20]. Therefore, VNCa can completely distinguish between OBM and BI. In addition, the use of pre-contrast VNCa to identify OBM and BI avoids the risk of adverse reactions that may arise from the use of iodine contrast agents, while only one phase of scanning greatly reduces the radiation dose to the patient.

BI are asymptomatic hamartoma malformations defined histologically as discrete lesions of dense bone within a cavernous membrane [31]. OBM are characterized by dysplasia of bone-like tissue with abundant tumor cells and incomplete deposition of calcium salts [20]. OBM do not contain normal cortical bone structure and their density is relatively lower than that of BI [33]. In our study, the mean CTa of OBM (526.70 ± 103.67 Hu) was significantly lower than BI (1030.18 ± 147.41 Hu), which is consistent with histology [33] and with the results of previous studies [18; 19]. We found that the IC of OBM (9.38 ± 2.13 mg/ml) was significantly lower than BI (18.14 ± 3.19 mg/ml ($P < 0.001$)). IC performed well in the

differential diagnosis of OBM and BI, with an AUC of 0.99 in the training group and AUC of 0.98 in the testing group. λ_{HU} represents the rate of decay change of the material. Consistent with the studies by Dong et al. [20] and Luo et al. [7], we found that BI had a significantly steeper slope than OBM. This indicates that the rate of change of attenuation is faster for BI than for OBM under different ray energies, which is likely related to their different structural compositions and physical properties.

Z_{eff} reflects the atomic number of a compound or mixture [34]; the denser the compound or mixture, the higher the Z_{eff} [35; 36]. Rho can distinguish between different substances by measuring their structure, physical and chemical properties [37]. It has been reported that Rho/Z_{eff} is highly accurate for identifying the composition of substances [38; 39]. Rho/Z_{eff} images have good diagnostic value in assessing bone marrow infiltration in primary malignant bone tumors [26]. We found that the mean Rho/Z_{eff} of BI was significantly higher than that of OBM, which is consistent with previous studies [11]. This indicates that the density of BI is higher than that of OBM.

This study has several limitations. First, this is a retrospective study with a relatively small sample size and possible selection bias. Second, most lesions were diagnosed through the findings of typical imaging modalities (CT, MRI, PET/PETCT) and by follow-up imaging, rather than by pathological examination of the tissue. Third, both (OBM and BI) groups were composed of different primary tumors. Due to the small sample size, subgroups of OBM and BI from different primary diseases could not be compared. The identification and analysis of OBM and BI should be further verified and explored using a larger population and a prospective multi-center study in the future.

Conclusions

The performance of DECT-derived quantitative parameters was effective for differentiating between OBM and BI. Specifically, pre-contrast VNCa has the best performance and can completely distinguish OBM from BI.

Abbreviations

AUC Area under the receiver operating characteristic curve

BI Bone islands

BM Bone metastasis

DECT Dual-energy computed tomography

OBM Osteoblastic metastasis

PET Positron emission tomography

ROC Receiver operating characteristic

SPECT Single photon emission computed tomography

VNCa Virtual non-calcium

Declarations

All manuscripts must contain the following sections under the heading 'Declarations':

Ethics approval and consent to participate

The study was conducted in accordance with the Declaration of Helsinki. This study was approved by the Institutional Review Board of Chongqing University Cancer Hospital and the need for written informed consent was waived owing to the use of retrospective data.

Consent for publication

Not applicable.

Competing interests

The authors declare that they have no known competing financial interests or personal relationships that could have appeared to influence the work reported in this paper.

Funding

This study has received funding by the Fundamental Research Funds for the Central Universities (2023CDJYGRH-YB04), the Chongqing University Cancer Hospital Scientific Research Capacity Improvement Project (2023nlts004), the Natural Science Foundation of Chongqing municipality (CSTB2023NSCQ-MSX0787, CSTB2024NSCQ-MSX0760), Chongqing Medical Research Project of Combination of Science and Medicine (No. 2024MSXM171).

Author Contribution

J.F.S. and J.H.S. collected and organized materials and the literature. M. L, J.Z, Y.T and H.Y extracted and interpreted the patient data. J.F.S., Y. H, Y.C and H.C. analyzed the results. J.F.S. and J.H.S. wrote the manuscript. L.W, X.W. and J.Z. revised the manuscript. X.W. and J.Z. provided technical support and verified all the data in the study. X.W. and J.Z. had final responsibility for the decision to submit for publication. All authors read and approved the final manuscript.

Acknowledgement

We thank the participants and referring technicians for their selfless and valuable assistance in this study.

Data Availability

The datasets generated and/or analyzed during the current study are not publicly available due to institutional and patient privacy restrictions but are available from the corresponding author on reasonable request.

References

1. Amoretti N, Thariat J, Nouri Y, et al. Sémiologie des métastases osseuses en radiologie conventionnelle. Bull Cancer. 2013;100:1109–14.
2. Yildizhan S, Boyaci MG, Rakip U, Aslan A, Canbek I. Role of radiofrequency ablation and cement injection for pain control in patients with spinal metastasis. BMC Musculoskelet Disord. 2021;22:912.
3. McCabe FJ, Jadaan MM, Byrne F, Devitt AT, McCabe JP. Spinal metastasis: The rise of minimally invasive surgery. Surgeon. 2022;20:328–33.
4. von Moos R, Costa L, Gonzalez-Suarez E, Terpos E, Niepel D, Body JJ. Management of bone health in solid tumours: From bisphosphonates to a monoclonal antibody. Cancer Treat Rev. 2019;76:57–67.
5. Coleman R, Hadji P, Body JJ, et al. Bone health in cancer: ESMO Clinical Practice Guidelines. Ann Oncol. 2020;31:1650–63.
6. Coleman RE, Croucher PI, Padhani AR, et al. Bone metastases. Nat Rev Dis Primers. 2020;6:83.
7. Luo H, Zou L, Yang Q, et al. Spectral CT assists differentiation of osteoblastic bone metastasis from bone island in newly diagnosed cancer patients. Eur Radiol. 2024;34:60–8.
8. Onitsuka H. Roentgenologic aspects of bone islands. Radiology. 1977;123:607–12.
9. Caballes RL, Caballes RA Jr. Polyostotic giant enostoses with strongly positive radionuclide bone scan. Ann Diagn Pathol. 2004;8:247–51.
10. Hong JH, Jung JY, Jo A, et al. Development and Validation of a Radiomics Model for Differentiating Bone Islands and Osteoblastic Bone Metastases at Abdominal CT. Radiology. 2021;299:626–32.
11. Xu C, Kong L, Deng X. Dual-Energy Computed Tomography For Differentiation Between Osteoblastic Metastases and Bone Islands. Front Oncol. 2022;12:815955.
12. Xiong Y, Guo W, Liang Z, et al. Deep learning-based diagnosis of osteoblastic bone metastases and bone islands in computed tomograph images: a multicenter diagnostic study. Eur Radiol. 2023;33:6359–68.
13. Aran S, Shaqdan KW, Abujudeh HH. Dual-energy computed tomography (DECT) in emergency radiology: basic principles, techniques, and limitations. Emerg Radiol. 2014;21:391–405.

14. Franco PN, Spasiano CM, Maino C et al. (2023) Principles and Applications of Dual-Layer Spectral CT in Gastrointestinal Imaging. Diagnostics (Basel) 13.
15. McCollough CH, Leng S, Yu L, Fletcher JG. Dual- and Multi-Energy CT: Principles, Technical Approaches, and Clinical Applications. Radiology. 2015;276:637–53.
16. Chung R, Dane B, Yeh BM, Morgan DE, Sahani DV, Kambadakone A. Dual-Energy Computed Tomography: Technological Considerations. Radiol Clin North Am. 2023;61:945–61.
17. Ulano A, Bredella MA, Burke P, et al. Distinguishing Untreated Osteoblastic Metastases From Enostoses Using CT Attenuation Measurements. AJR Am J Roentgenol. 2016;207:362–8.
18. Elangovan SM, Sebro R. Accuracy of CT Attenuation Measurement for Differentiating Treated Osteoblastic Metastases From Enostoses. AJR Am J Roentgenol. 2018;210:615–20.
19. Sala F, Dapoto A, Morzenti C, et al. Bone islands incidentally detected on computed tomography: frequency of enostosis and differentiation from untreated osteoblastic metastases based on CT attenuation value. Br J Radiol. 2019;92:20190249.
20. Dong Y, Zheng S, Machida H, et al. Differential diagnosis of osteoblastic metastases from bone islands in patients with lung cancer by single-source dual-energy CT: advantages of spectral CT imaging. Eur J Radiol. 2015;84:901–7.
21. Lin S-C, Yu-Lee L-Y, Lin S-H. Osteoblastic Factors in Prostate Cancer Bone Metastasis. Curr Osteoporos Rep. 2018;16:642–7.
22. Yang W, Pan Q, Huang F, Hu H, Shao Z. Research progress of bone metastases: From disease recognition to clinical practice. Front Oncol. 2022;12:1105745.
23. Hensel J, Thalmann GN. Biology of Bone Metastases in Prostate Cancer. Urology. 2016;92:6–13.
24. Sung H, Ferlay J, Siegel RL, et al. Global Cancer Statistics 2020: GLOBOCAN Estimates of Incidence and Mortality Worldwide for 36 Cancers in 185 Countries. CA Cancer J Clin. 2021;71:209–49.
25. Mallinson PI, Coupal TM, McLaughlin PD, Nicolaou S, Munk PL, Ouellette HA. Dual-Energy CT for the Musculoskeletal System. Radiology. 2016;281:690–707.
26. Liu S, Pan H, Wu S, et al. Diagnostic Value of Dual-Energy CT Virtual Non-Calcium and Rho/Z Images for Bone Marrow Infiltration in Primary Malignant Bone Tumors. Acad Radiol. 2023;30:1659–66.
27. Kosmala A, Weng AM, Heidemeier A, et al. Multiple Myeloma and Dual-Energy CT: Diagnostic Accuracy of Virtual Noncalcium Technique for Detection of Bone Marrow Infiltration of the Spine and Pelvis. Radiology. 2018;286:205–13.
28. Abdullayev N, Grosse Hokamp N, Lennartz S, et al. Improvements of diagnostic accuracy and visualization of vertebral metastasis using multi-level virtual non-calcium reconstructions from dual-layer spectral detector computed tomography. Eur Radiol. 2019;29:5941–9.
29. undefined u, undefined u, undefined u. (2018) The Ability of Dual-Energy Computed Tomography to Distinguish Normal Bone Marrow From Metastases Using Bone Marrow Color Maps. J Comput Assist Tomogr 42.

30. Shi J, Huang H, Xu S, et al. XGBoost-based multiparameters from dual-energy computed tomography for the differentiation of multiple myeloma of the spine from vertebral osteolytic metastases. Eur Radiol. 2023;33:4801–11.
31. Greenspan A. Bone island (enostosis): current concept–a review. Skeletal Radiol. 1995;24:111–5.
32. Greenspan A, Steiner G, Knutzon R. Bone island (enostosis): clinical significance and radiologic and pathologic correlations. Skeletal Radiol. 1991;20:85–90.
33. Clezardin P, Teti A. Bone metastasis: pathogenesis and therapeutic implications. Clin Exp Metastasis. 2007;24:599–608.
34. Shen H, Yuan X, Liu D, et al. Multiparametric dual-energy CT for distinguishing nasopharyngeal carcinoma from nasopharyngeal lymphoma. Eur J Radiol. 2021;136:109532.
35. Garcia LI, Azorin JF, Almansa JF. A new method to measure electron density and effective atomic number using dual-energy CT images. Phys Med Biol. 2016;61:265–79.
36. Mileto A, Allen BC, Pietryga JA, et al. Characterization of Incidental Renal Mass With Dual-Energy CT: Diagnostic Accuracy of Effective Atomic Number Maps for Discriminating Nonenhancing Cysts From Enhancing Masses. AJR Am J Roentgenol. 2017;209:W221–30.
37. Tolborg K, Iversen BB. Electron Density Studies in Materials Research. Chemistry. 2019;25:15010–29.
38. Tatsugami F, Higaki T, Kiguchi M, et al. Measurement of electron density and effective atomic number by dual-energy scan using a 320-detector computed tomography scanner with raw data-based analysis: a phantom study. J Comput Assist Tomogr. 2014;38:824–7.
39. Schaeffer CJ, Leon SM, Olguin CA, Arreola MM. Accuracy and reproducibility of effective atomic number and electron density measurements from sequential dual energy CT. Med Phys. 2021;48:3525–39.

Figures

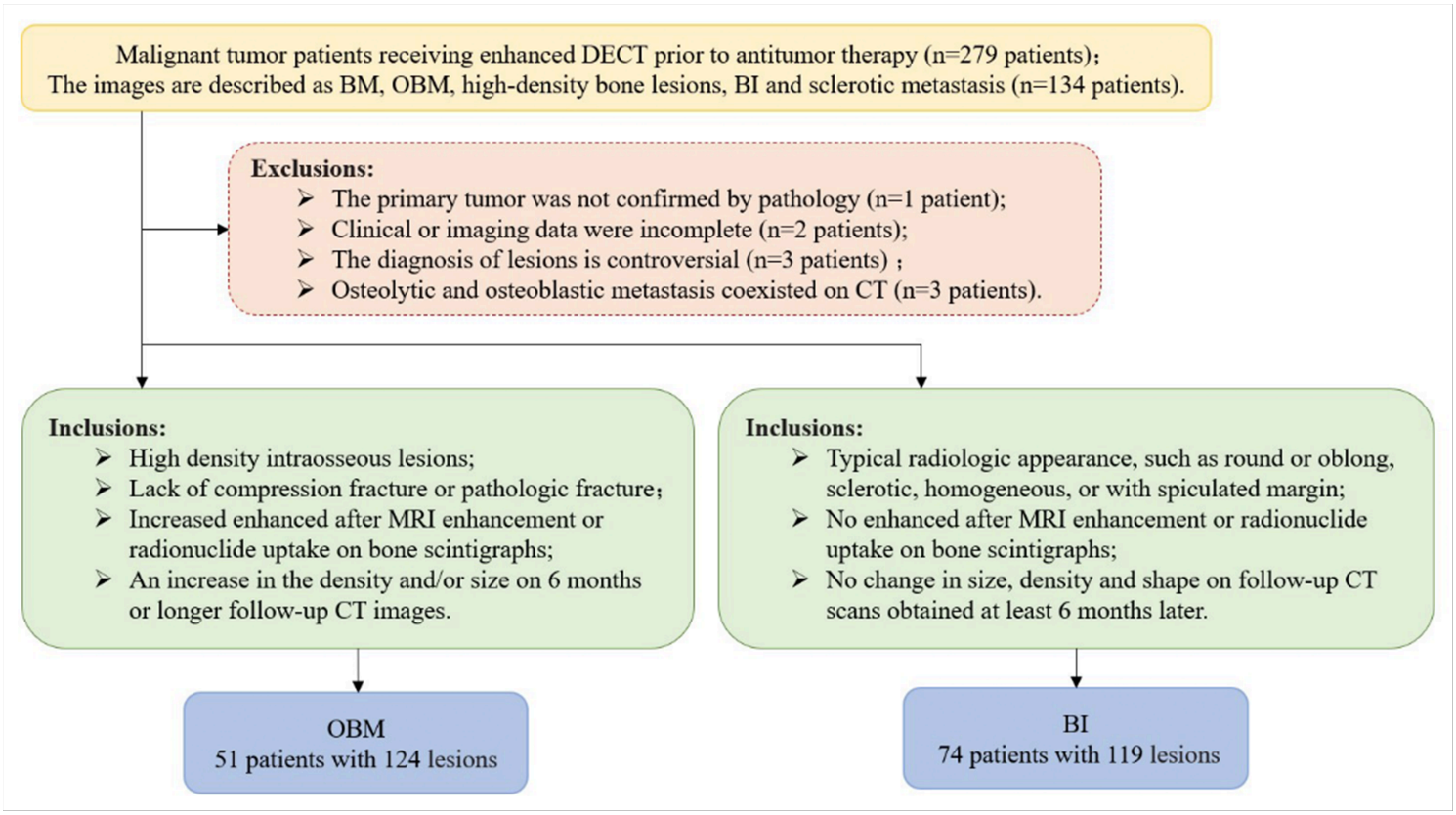


Figure 1

Flow chart demonstrating the selection process of the study population. BI, Bone islands; BM, bone metastasis; DECT, dual-energy computed tomography; OBM, Osteoblastic metastasis.

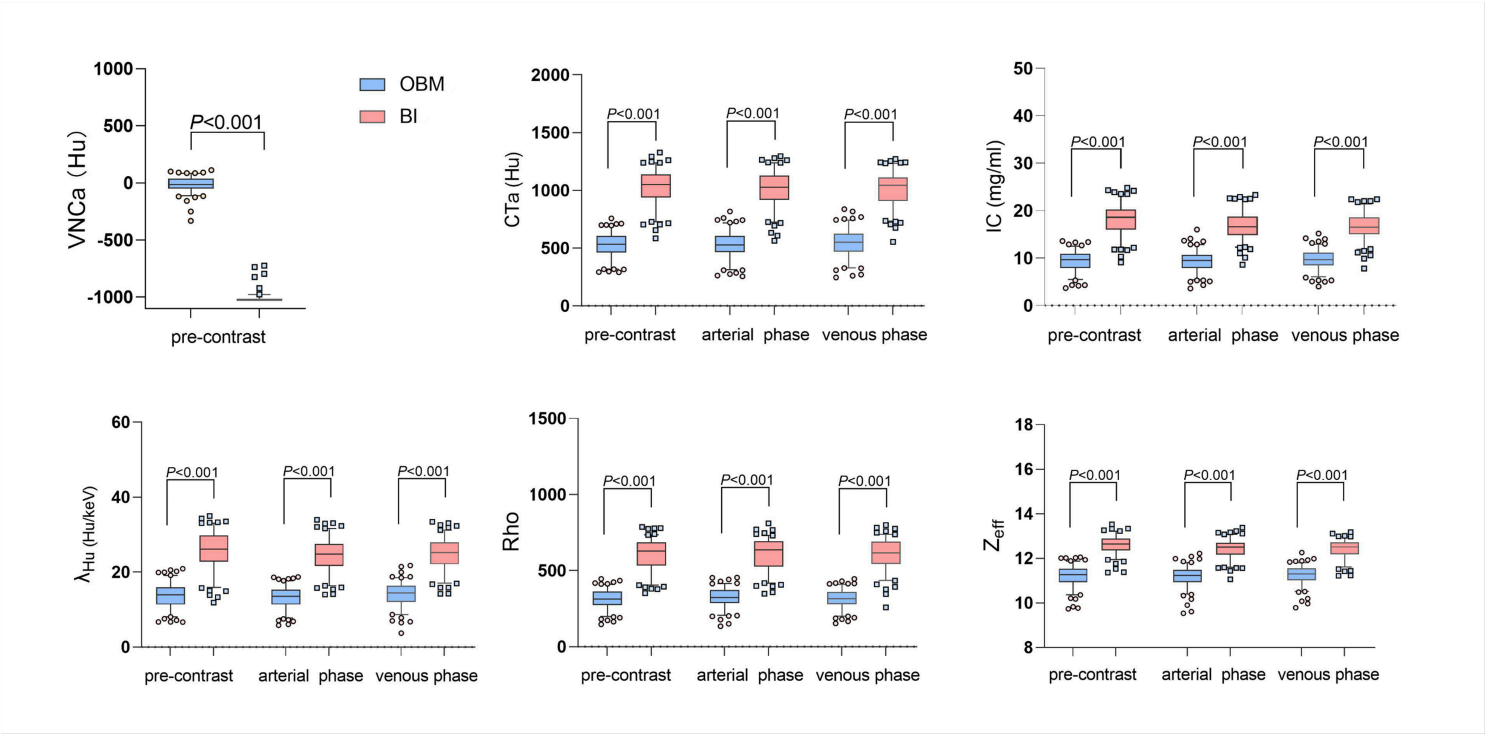


Figure 2

Box-and-whisker plots presenting the distributions of DECT quantitative parameters. BI, Bone islands; CTa, CT attenuation; Hu, Hounsfield unit; IC, Iodine concentration; Rho, electron density; OBM, Osteoblastic metastasis; VNCa, virtual non-calcium; Z_{eff}, effective atomic number; λ_{Hu}, slope of the spectral Hounsfield unit curve.

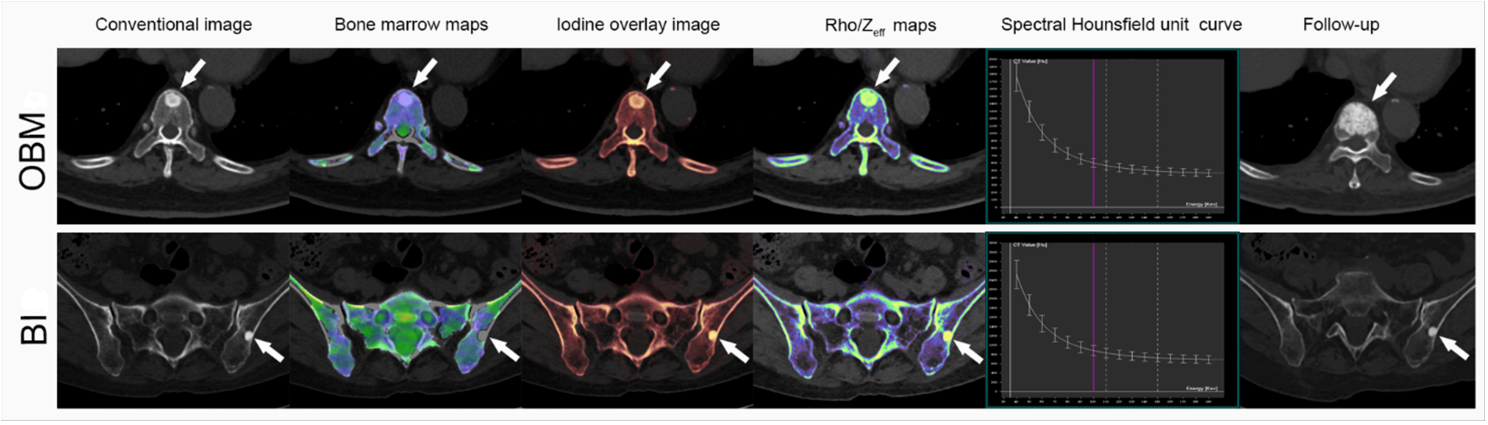


Figure 3

Representative DECT images. OBM: Patients with primary lesions of prostate cancer. At follow-up CT imaging 16 months later, the size and density of intraosseous focal high-density lesions were increased, and the lesion was diagnosed as OBM. BI: Patients with primary lesions of sigmoid cancer. At follow-up CT imaging 8 months later, the size and density of intraosseous focal high-density lesions had not changed, and the lesion was diagnosed as BI. BI, Bone islands; DECT, dual-energy computed tomography; OBM, Osteoblastic metastasis; Rho, electron density; Z_{eff}, effective atomic number.

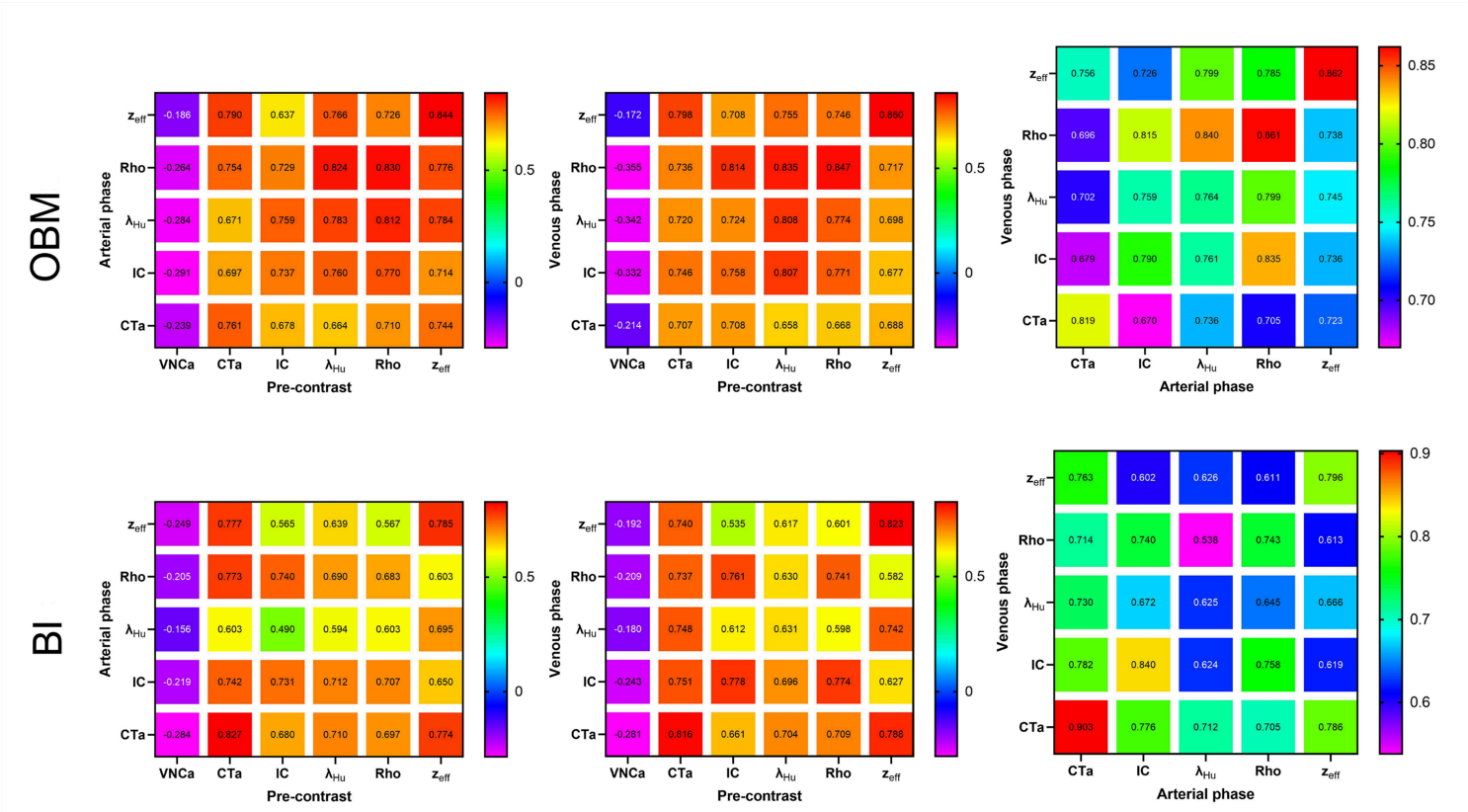


Figure 4

Correlation heatmaps between different phases in the OBM group and BI group. BI, Bone islands; CTa, CT attenuation; IC, Iodine concentration; OBM, Osteoblastic metastasis; Rho, electron density; VNCa, virtual non-calcium; Z_{eff}, effective atomic number; λ_{Hu}, slope of the spectral Hounsfield unit curve.

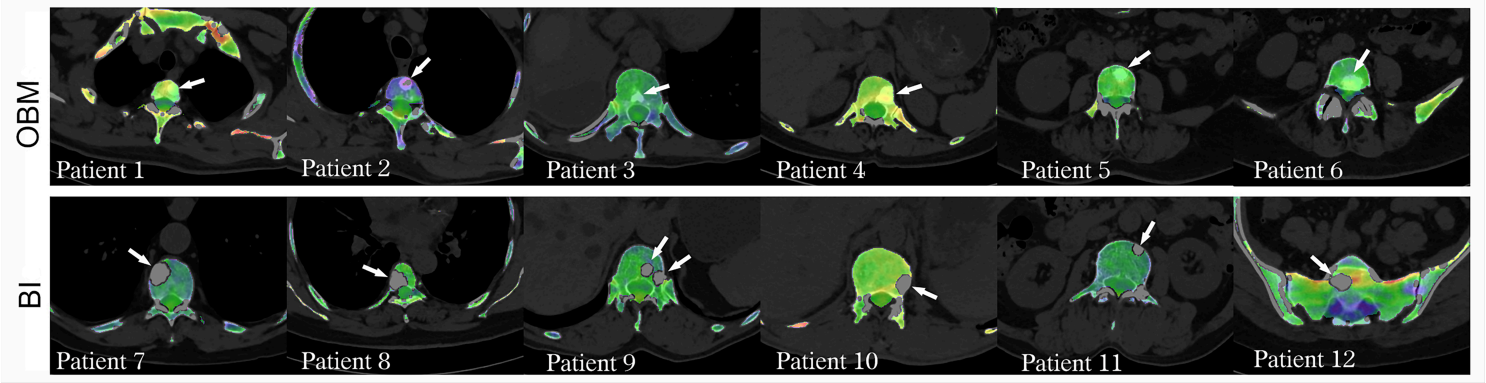


Figure 5

Representative DECT bone marrow images. BI, Bone islands; DECT, dual-energy computed tomography; OBM, Osteoblastic metastasis.

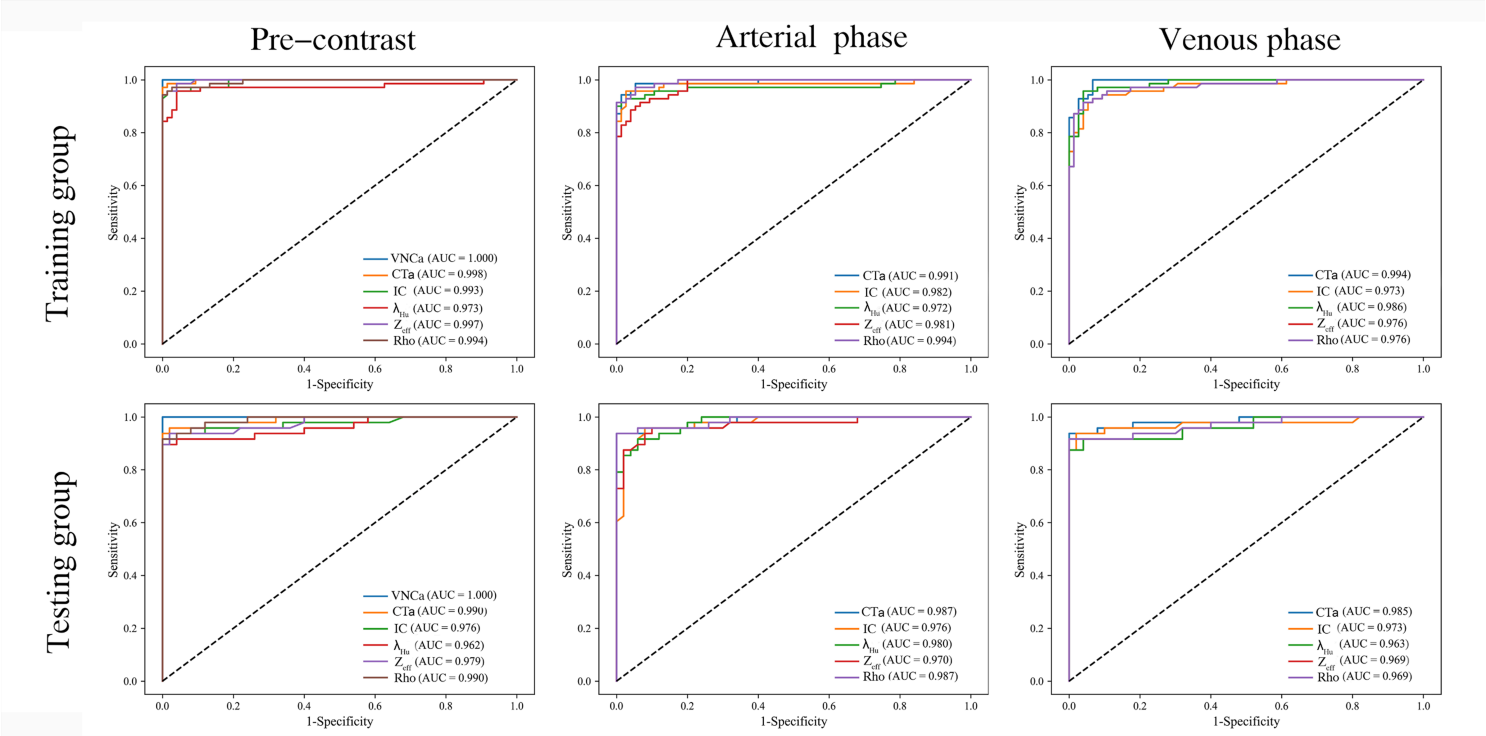


Figure 6

Receiver operating characteristic curves of DECT quantitative parameters in the training group and testing group. AUC, area under the receiver operating characteristic curve; CTa, CT attenuation; Hu,

Hounsfield unit; IC, Iodine concentration; Rho, electron density; ROC, receiver operating characteristic; VNCa, virtual non-calcium; Z_{eff}, effective atomic number; λ_{Hu}, slope of the spectral Hounsfield unit curve.

Supplementary Files

This is a list of supplementary files associated with this preprint. Click to download.

- Table1.docx
- Table3.docx
- Table2.docx